



Early Results from GLASS-JWST. III. Galaxy Candidates at $z \sim 9-15^*$

Marco Castellano¹, Adriano Fontana¹, Tommaso Treu², Paola Santini¹, Emiliano Merlin¹, Nicha Leethochawalit^{3,4,5}, Michele Trenti^{3,4}, Eros Vanzella⁶, Uros Mestric⁶, Andrea Bonchi⁷, Davide Belfiori¹, Mario Nonino⁸, Diego Paris¹, Gianluca Polenta⁷, Guido Roberts-Borsani², Kristan Boyett^{3,4}, Maruša Bradac^{9,10}, Antonello Calabrò¹, Karl Glazebrook¹¹, Claudio Grillo^{12,13}, Sara Mascia¹, Charlotte Mason^{14,15}, Amata Mercurio¹⁶, Takahiro Morishita¹⁷, Themiya Nanayakkara¹¹, Laura Pentericci¹, Piero Rosati^{18,19}, Benedetta Vulcani²⁰, Xin Wang²¹, and Lilan Yang²²

¹ INAF—Osservatorio Astronomico di Roma, via di Frascati 33, I-00078 Monte Porzio Catone, Italy; marco.castellano@inaf.it

² Department of Physics and Astronomy, University of California, Los Angeles, 430 Portola Plaza, Los Angeles, CA 90095, USA

³ School of Physics, University of Melbourne, Parkville 3010, VIC, Australia

⁴ ARC Centre of Excellence for All Sky Astrophysics in 3 Dimensions (ASTRO 3D), Australia

⁵ National Astronomical Research Institute of Thailand (NARIT), Mae Rim, Chiang Mai, 50180, Thailand

⁶ INAF—OAS, Osservatorio di Astrofisica e Scienza dello Spazio di Bologna, via Gobetti 93/3, I-40129 Bologna, Italy

⁷ Space Science Data Center, Italian Space Agency, via del Politecnico, I-00133, Roma, Italy

⁸ INAF—Osservatorio Astronomico di Trieste, Via Tiepolo 11, I-34131 Trieste, Italy

⁹ University of Ljubljana, Department of Mathematics and Physics, Jadranska ulica 19, SI-1000 Ljubljana, Slovenia

¹⁰ Department of Physics and Astronomy, University of California Davis, 1 Shields Avenue, Davis, CA 95616, USA

¹¹ Centre for Astrophysics and Supercomputing, Swinburne University of Technology, PO Box 218, Hawthorn, VIC 3122, Australia

¹² Dipartimento di Fisica, Università degli Studi di Milano, via Celoria 16, I-20133 Milano, Italy

¹³ INAFIASF Milano, via A. Corti 12, I-20133 Milano, Italy

¹⁴ Cosmic Dawn Center (DAWN), Denmark

¹⁵ Niels Bohr Institute, University of Copenhagen, Jagtvej 128, DK-2200 København N, Denmark

¹⁶ INAF—Osservatorio Astronomico di Capodimonte, Via Moiariello 16, I-80131 Napoli, Italy

¹⁷ IPAC, California Institute of Technology, MC 314-6, 1200 E. California Boulevard, Pasadena, CA 91125, USA

¹⁸ Dipartimento di Fisica e Scienze della Terra, Università degli Studi di Ferrara, Via Saragat 1, I-44122 Ferrara, Italy

¹⁹ INAF—OAS, Osservatorio di Astrofisica e Scienza dello Spazio di Bologna, via Gobetti 93/3, I-40129 Bologna, Italy

²⁰ INAF Osservatorio Astronomico di Padova, vicolo dell'Osservatorio 5, I-35122 Padova, Italy

²¹ Infrared Processing and Analysis Center, Caltech, 1200 E. California Blvd., Pasadena, CA 91125, USA

²² Kavli Institute for the Physics and Mathematics of the Universe, The University of Tokyo, Kashiwa, 277-8583, Japan

Received 2022 July 19; revised 2022 September 24; accepted 2022 September 26; published 2022 October 18

Abstract

We present the results of a first search for galaxy candidates at $z \sim 9-15$ on deep seven-band NIRCcam imaging acquired as part of the GLASS-James Webb Space Telescope (JWST) Early Release Science Program on a flanking field of the Frontier Fields cluster A2744. Candidates are selected via two different renditions of the Lyman-break technique, isolating objects at $z \sim 9-11$, and $z \sim 9-15$, respectively, supplemented by photometric redshifts obtained with two independent codes. We find five color-selected candidates at $z > 9$, plus one additional candidate with photometric redshift $z_{\text{phot}} \geq 9$. In particular, we identify two bright candidates at $M_{\text{UV}} \simeq -21$ that are unambiguously placed at $z \simeq 10.6$ and $z \simeq 12.2$, respectively. The total number of galaxies discovered at $z > 9$ is in line with the predictions of a nonevolving luminosity function. The two bright ones at $z > 10$ are unexpected given the survey volume, although cosmic variance and small number statistics limits general conclusions. This first search demonstrates the unique power of JWST to discover galaxies at the high-redshift frontier. The candidates are ideal targets for spectroscopic follow-up in Cycle-2.

Unified Astronomy Thesaurus concepts: [Reionization \(1383\)](#)

1. Introduction

Since the discovery of the first object at a cosmological distance (Schmidt 1963), the quest for “the most distant source ever seen” has been both a motivation and a powerful means to expand our understanding of cosmology and of how astronomical objects formed and evolved. Substantial progress in the study of distant, star-forming galaxies has been enabled by the Lyman-break technique yielding to samples of so-called

Lyman-break galaxies (LBGs) at progressively higher redshifts (e.g., Giavalisco 2002).

In recent years, the combination of Hubble Space Telescope (HST) and ground-based data enabled the selection of relatively large samples of LBGs at $z \sim 2-8$ (e.g., Reddy & Steidel 2009; McLure et al. 2013; Finkelstein et al. 2015; Roberts-Borsani et al. 2016; Atek et al. 2018; Ono et al. 2018). The inferred UV luminosity functions (LF), together with assumptions on the ionizing output of LBGs, enabled the first investigations of the epoch of reionization (e.g., Dayal & Ferrara 2018). The data are consistent with a scenario in which the universe was still largely neutral at $z \sim 8$ and was rapidly reionized by $z \sim 5.5-6$ (e.g., Mitra et al. 2015; Greig & Mesinger 2017; Mason et al. 2018), likely by faint star-forming galaxies (e.g., Castellano et al. 2016b; Yue et al. 2018; Finkelstein et al. 2019; Dayal et al. 2020).

* Based on observations collected with JWST under the ERS program ID 1324 (PI T. Treu).



Very few constraints are available at higher redshifts. Small samples of increasingly bright objects have been selected up to $z \sim 9\text{--}11$ (Zheng et al. 2012; Coe et al. 2013; Oesch et al. 2013; McLeod et al. 2016; Hashimoto et al. 2018; Ishigaki et al. 2018; Morishita et al. 2018; Rojas-Ruiz et al. 2020; Bouwens et al. 2021; Bagley et al. 2022; Roberts-Borsani et al. 2022a). The available estimates of the Schechter UV LF show significant discrepancies, with some results in agreement with a smooth evolution from lower redshifts, driven either by a decrease of ϕ^* or by a dimming of M^* (e.g., McLeod et al. 2016), and other analyses suggesting either a dearth (Oesch et al. 2018) or an excess (Bagley et al. 2022) of bright galaxies at $z \sim 10$. As a result, the cosmic star formation rate (SFR) density is poorly constrained, and it is not clear whether the ratio between SFR and dark matter accretion rate remains approximately constant at $z \sim 9\text{--}11$ as found at $z \lesssim 7$ (Harikane et al. 2022a).

The discovery of the population of galaxies that ended the so-called *dark ages* at $z \sim 12$ and beyond has been so far prevented by the limited IR spectral coverage of HST, and by the insufficient sensitivity and resolution of Spitzer and ground-based telescopes. In fact, at such high redshifts, only tentative candidates have been found (Harikane et al. 2022a). The highest spectroscopically confirmed redshift is that of LBG GN-z11 at $z = 10.957$ (Oesch et al. 2016; Jiang et al. 2021). Even with their limitations, current observations have challenged our understanding of galaxy buildup in the early universe. The number densities of bright $z > 10$ candidates and GN-z11 lie above the typical empirical Schechter function (e.g., Bowler et al. 2020) while theoretical models are in tension with the abundance of bright galaxies (Finkelstein et al. 2022). Thus, these remarkably bright galaxies may mark a significant transition in the mode of galaxy formation in the early universe: likely significantly less dust-obscured and with a higher star formation efficiency enabling more stars to form in high-mass halos, and/or the presence of young quasars. Understanding how these galaxies formed requires building a census of the galaxy population at $z > 10$ with deeper photometric data, especially at longer wavelengths than those covered by HST.

In this paper we present the search for LBG candidates at $z \sim 9\text{--}15$ in the first NIRCcam imaging data from the GLASS-James Webb Space Telescope (JWST) Early Release Science Program (JWST-ERS-1324; Treu et al. 2022, hereafter T22). GLASS-JWST targets the Hubble Frontier Fields (HFF) galaxy cluster A2744 (Lotz et al. 2014; Castellano et al. 2016a; Merlin et al. 2016a) with NIRISS and NIRSpec spectroscopy, while obtaining coordinated parallel observations with NIRCcam on two flanking fields. The GLASS NIRCcam parallels are the deepest images collected by the 13 ERS programs. Details on the design and strategy of the GLASS-JWST survey can be found in T22. Throughout the paper, we adopt AB magnitudes (Oke & Gunn 1983), and a flat Λ -cold-dark-matter concordance model ($H_0 = 70.0 \text{ km s}^{-1} \text{ Mpc}^{-1}$, $\Omega_M = 0.30$).

2. GLASS-JWST NIRCcam Imaging

The GLASS-JWST NIRCcam observations discussed in this paper were taken in parallel to NIRISS on 2022 June 28–29. They are centered at R.A. = 3.5017025 deg and decl. = -30.3375436 deg, and consist of images in seven bands: F090W (total exposure time 11,520 s), F115W (11,520 s), F150W (6120 s), F200W (5400 s), F277W

(5400 s), F356W (6120 s), and F444W (23,400 s). The image reduction and calibration, and the methods used to detect sources and measure multiband photometry are described in a companion paper (Paper II in this series, Merlin et al. 2022, hereafter M22). The NIRISS observations are described in Paper I (Roberts-Borsani et al. 2022b).

For the convenience of the reader, we briefly summarize below the information relevant for the present paper. Data reduction and flux calibration were obtained using the official JWST pipeline²³ and exploiting the calibration files made available by STScI on 2022 July 29. A customized step has been introduced to improve masking of image defects (*snowballs* and *wisps*) and to improve the subtraction of $1/f$ noise and background. Images have been aligned to a common reference grid (defined on Gaia Data Release 3 calibrated ground-based images) using a custom pipeline already adopted in similar projects (Fontana et al. 2014).

We warn the reader that flat-fielding, flux calibration, and other steps of the data processing are inevitably based on preliminary calibrations. Similarly, the cleaning of defects, especially in the bluest bands that are used here to identify the Lyman break, will also be improved as the knowledge of the telescope and instrument improves.

Objects were detected using a customized version of SEXTRACTOR (Bertin & Arnouts 1996; Guo et al. 2013, v2.8.6) on the F444W coadded image. Total F444W fluxes in elliptical apertures as defined by Kron (1980) were measured with A-PHOT (Merlin et al. 2019). Fluxes in the other bands were measured with A-PHOT in several apertures at the positions of the detected sources using images point-spread function-matched to the F444W one. For the final search of high- z candidates, we have used both an aperture of 2FWHM diameter ($=0''.28$) as well as a smaller, $0''.2$ one. The latter has been adopted to optimize the search of potentially blended sources, which may be useful in our crowded field.

The final 5σ depths for point sources within a circular aperture of diameter of $0''.2$ are 28.78, 29.03, 28.84, 28.89, 29.26, 29.33, 29.71 in the F090W – F444W bands, respectively (M22). We estimate a total area of $\sim 7 \text{ arcmin}^2$ available for the selection of high-redshift candidates by considering the regions observed in all bands, and excluding the pixels occupied by foreground sources. Modest lensing magnification is expected to be present in the NIRCcam parallel fields. In this initial set of papers, we neglect the effect. The issue will be revisited after the completion of the campaign, which includes a second NIRCcam field, in parallel to NIRSpec observations (T22).

3. Selection of Lyman-break Galaxies at $z > 9$ with NIRCcam

3.1. Color–Color Selection

We defined the color selection criteria for galaxies at $z \sim 9\text{--}15$ using a catalog of objects at $z = 0\text{--}15$ that mimics our observations. The catalog comprises objects at $0 < z \leq 4.5$ generated with the Empirical Galaxy Generator (EGG) code (Schreiber et al. 2017a), which is based on empirical relations to reproduce observed number counts and color distributions of galaxies at low and intermediate redshifts. Galaxies at higher redshifts have been generated according to observed UV LFs

²³ <https://jwst-docs.stsci.edu/jwst-science-calibration-pipeline-overview>

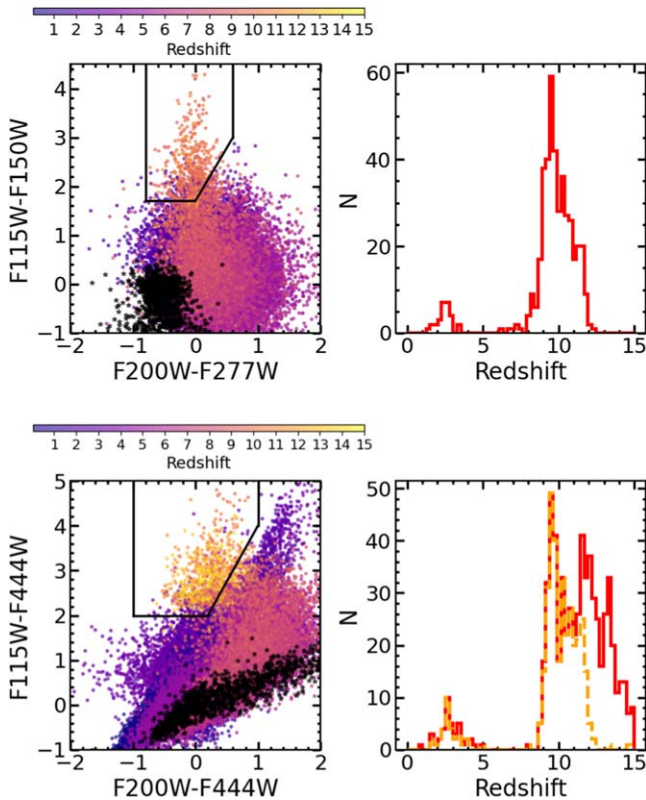


Figure 1. Color selection diagrams (left panels), and redshift distribution of selected galaxies (right panels), for LBGs at $z \sim 9\text{--}11$ (top, selection (1)) and $z \sim 9\text{--}15$ (bottom, selection (2)) exploiting the NIRCcam filters of the GLASS-JWST-ERS parallel. The catalog comprises objects at $z = 0\text{--}15$ over an area of 0.12 deg^2 . Black stars show the position of brown dwarf models from Marley et al. (2021) normalized at $26.0 \leq F444W \leq 28.0$ that meet our detection criteria for high-redshift galaxies. All fluxes have been perturbed with realistic noise properties.

over $z \sim 5\text{--}10$ (McLeod et al. 2015; Oesch et al. 2018; Bouwens et al. 2021) and randomly associating to each object a template from a library based on Bruzual & Charlot (2003, hereafter BC03) models with metallicity = $0.02, 0.2 Z_{\odot}$, $0 < E(B - V) < 0.2$, constant SFH, Salpeter (1955) initial mass function, and Calzetti et al. (2000) extinction law to predict photometry in 7 bands.

In order to provide sufficient statistics to design appropriate selection criteria, we simulated the catalog over an area of $\sim 0.12 \text{ deg}^2$, which is ~ 60 times larger than the NIRCcam parallel field, and we assumed no evolution of the UV LF beyond $z = 10$. We also artificially boosted the number counts at $z > 9.5$ by a factor of 20. The overrepresentation of high- z sources in the mock catalogs is taken into account when considering purity and completeness. Late-type dwarf stars are another potential source of contamination for the color selection of high-redshift galaxies. We assessed their impact using synthetic JWST photometry for the models by Marley et al. (2021), which include brown dwarfs and self-luminous extrasolar planets with $200 \leq T_{\text{eff}} \leq 2400$ and metallicity $[M/H]$ from 0.5 to +0.5. The brown dwarf models were normalized at $26.0 \leq F444W \leq 28.0$ in 0.5 mag steps.

Finally, the catalogs were perturbed by adding noise in order to reproduce the expected relation and scatter between magnitudes and errors in each band.

We find that the following color-color selection window, which is a modified version of the selection proposed by

Hainline et al. (2020), identifies objects at $z \sim 9\text{--}11.5$, as shown also in the top panels of Figure 1:

$$\begin{aligned} (F115W - F150W) &> 1.7, \\ (F115W - F150W) &> 2.17 \times (F200W - F277W) + 1.7, \\ -0.8 &< (F200W - F270W) < 0.6. \end{aligned} \quad (1)$$

In addition, we require a signal-to-noise ratio (S/N) > 3 in all bands redward of the Lyman break (F150W, F200W, F277W, F356W), and $S/N < 1.5$ in the F090W band.

Objects in the wider range $z \sim 9\text{--}15$ are well identified by the following selection criteria, which leverages also on the redder bands (e.g., F444W):

$$\begin{aligned} (F115W - F444W) &> 2.0, \\ (F115W - F444W) &> 2.5 \times (F200W - F444W) + 1.5, \\ -1.0 &< (F200W - F444W) < 1.0. \end{aligned} \quad (2)$$

By requiring all the S/N requirements above, plus $S/N(F150W) < 2$ and $S/N(F115W) < 2$, the selection in Equation (2) proves to be complementary to the one in Equation (1), sampling the $z \sim 11\text{--}15$ redshift range (Figure 1, bottom panels). We verified that most of the $z \lesssim 11$ objects selected in the F115W – F150W versus F200W – F277W diagram occupy the expected color space in F115W – F444W versus the F200W – F444W one, although photometric scatter may move them outside the color selection window. For this reason, and given also the differences in depths among the various bands, the two diagrams are not expected to select coincident samples in the $z \sim 9\text{--}11$ range.

For both color selections described above, we consider only objects with $S/N(F444W) > 8$, corresponding to $F444W \sim 28.2$, that, given the relevant depths in the bluer bands, enable the measurement of the large color terms ($\sim 1.7\text{--}2$) required to separate the high-redshift galaxies from the bulk of contaminants. While the proposed diagrams efficiently select high-redshift targets, some contamination from low-redshift galaxies is evident from the redshift distribution of the selected objects (right panels in Figure 1). The impact of such contamination and the completeness of the selection criteria will be discussed in Section 3.3. Instead, contamination from brown dwarfs is not a concern for our $z \sim 9\text{--}15$ selection. We show in Figure 1 late-type stars with $26.0 \leq F444W \leq 28.0$ that meet the above-mentioned S/N criteria in the F150W to F444W bands: the brown dwarfs occupy a distinct region of the color diagrams.

3.2. Photometric Redshift Selection

In addition, we search for high-redshift candidates that do not meet the color selection criteria defined above but have robust photometric redshift in the range $z = 9\text{--}15$. We estimate photometric redshifts with two different codes, EAZY (Brammer et al. 2008), and ZPHOT (Fontana et al. 2000). The EAZY code was run with the default V1.3 spectral template and a flat prior (see the companion paper by Leethochawalit et al. 2022). The analysis with ZPHOT has been performed by fitting the observed photometry with BC03 templates (see the companion paper by Santini et al. 2022). As described by Merlin et al. (2021), the BC03 library includes templates with both declining and delayed star formation histories and models the contribution from the nebular continuum and line emission

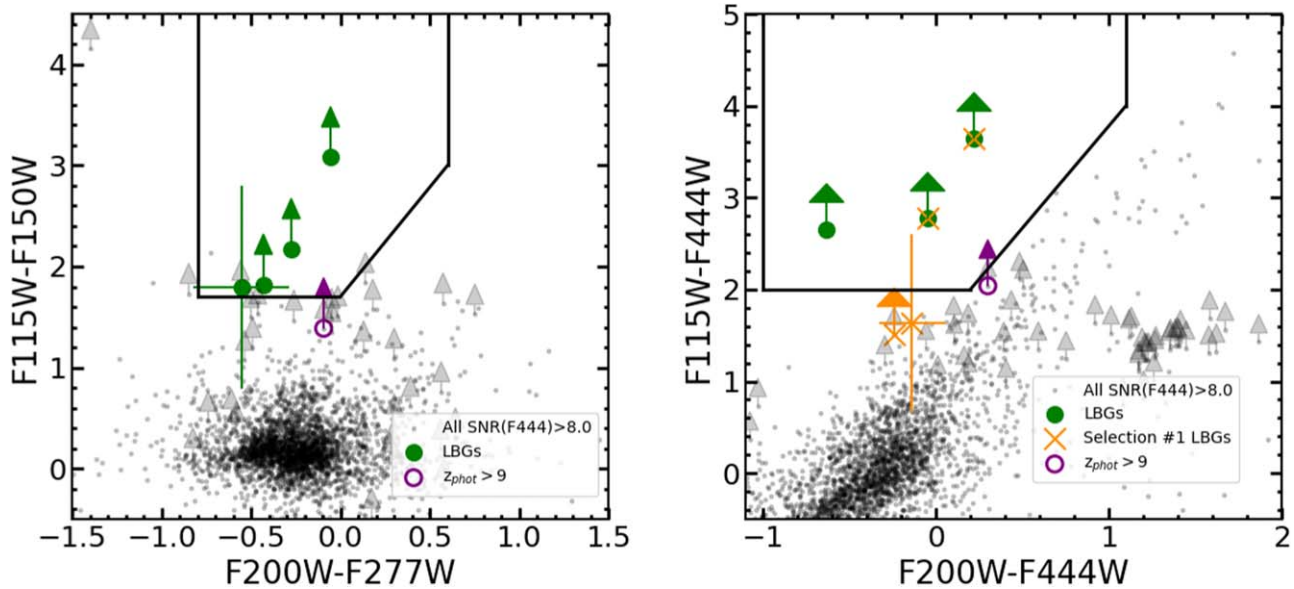


Figure 2. Observed color selection diagrams for LBGs at $z \sim 9$ –11 (left, selection (1)) and $z \sim 9$ –15 (right, selection (2)) in GLASS-JWST. Gray points show all objects with $S/N(F444W) > 8$ in the GLASS catalog. Green circles indicate the color-selected candidates. The additional candidate selected on the basis of photometric redshift is shown as a purple empty circle. The $z \sim 9$ –11 LBGs from the selection (1) diagram are shown as dark orange crosses in the selection (2) one. Upper limits are indicated by arrows. All error bars and upper limits are at 1σ .

following Schaerer & de Barros (2009) and Castellano et al. (2014).

Conservatively, photometric redshift candidates are chosen as objects with both $z_{\text{EAZY}} > 9$ and $z_{\text{phot}} > 9$.

We also require $S/N(F444W) > 8$ and $S/N > 3$ in F200W, F277W, and F356W to ensure a proper measurement of the spectral energy distributions (SEDs). Although some true positives may be lost with this approach, the multiple requirements help minimize the risk of contamination.

3.3. Completeness and Purity

We used simulations to estimate the completeness of our selection of $z > 9$ galaxies. First, simulated NIRCcam images in all relevant filters are built out of raw frames obtained by the MIRAGE²⁴ software on the basis of the actual scheduling of the program as derived from the Astronomers Proposal Tool. The simulations as described by M22 were used to fine tune the image reduction pipeline, and accurately reproduce the noise properties of the real NIRCcam images.

Second, we inserted in blank regions of the simulated images 2.5×10^5 mock LBGs at $9 < z < 15$ and with a constant distribution at $-18.5 < M_{\text{UV}} < -22.5$. The observed magnitudes are obtained by randomly associating a BC03 model from the library described in Section 3. We assume that objects follow a circular Sersic (1968) light profile with $n = 1$ and that their effective radius scales with L_{UV} as $r_e \propto L^{0.5}$, consistent with several estimates at comparable redshifts (e.g., Grazian et al. 2012; Kawamata et al. 2018; Bouwens et al. 2022; Yang et al. 2022a). Following Yang et al. (2022a), we assume an effective radius of 0.8 kpc for objects with $M_{\text{UV}} = -21$. In order to avoid overcrowding, simulations are repeated by inserting 500 objects each time. Detection and photometry on the simulated galaxies are performed in the same way as for the real catalog.

We estimate a completeness of $\sim 70\%$ ($\sim 60\%$) for the selection of bright $M_{\text{UV}} < -20$ objects at $z \sim 9$ –11 ($z \sim 11$ –15), decreasing to $\sim 60\%$ ($\sim 50\%$) at the nominal limits of $M_{\text{UV}} < -19.0$ (-19.5) quoted above. We also find a nonnegligible chance of detection of fainter targets due to photometric scatter, with a completeness of $\sim 50\%$ ($\sim 35\%$) for the selection of objects of $M_{\text{UV}} \sim -18.5$ (-19.0) at $z \sim 9$ –11 ($z \sim 11$ –15).

We evaluate potential contamination with two different mock catalogs perturbed with realistic noise reproducing the depth of our data. As a first test, we use the mock catalog described in Section 3 based on EGG and known UV LFs from the literature. We find that each of our color criteria would select ~ 0.6 interlopers on an area equivalent to ours. As expected (e.g., Vulcani et al. 2017), the interlopers are mostly faint ($F444W \sim 28$), red galaxies at $z \sim 2$ –3 (see Figure 1). As a second test we use the mock catalogs from the JAGUAR; Williams et al. 2018), including predicted NIRCcam fluxes for objects at $0.2 < z < 15$ and stellar mass $\log(M/M_{\odot}) > 6$. JAGUAR provides a complementary test with respect to EGG also thanks to the inclusion of emission lines in the predicted SEDs. The potential contamination from objects in the JAGUAR catalog turns out to be much lower than in the previous case, i.e., < 0.1 objects per selection, per field. In conclusion, both tests suggest that residual contamination should be small, albeit with some uncertainty. This is inevitable, considering that the 1–5 μm spectra of intermediate galaxies at these depths are uncharted territory.

4. Candidate Galaxies at $z = 9$ –15

The resulting observed color–color diagrams are shown in Figure 2. We select five candidates at $z > 9$ by combining the samples from the two selections described in Section 3. One additional candidate is selected from the photometric redshift analysis described in Section 3.2. The positions and magnitudes of the candidates are listed in Table 1. All objects are

²⁴ <https://www.stsci.edu/jwst/science-planning/proposal-planning-toolbox/mirage>

Table 1
Galaxy Candidates at $z > 9$ in GLASS-JWST-ERS^a

| ID | R.A. (deg.) | Decl. (deg.) | F444W | z_{EAZY} | z_{phot} | M_{UV} | β | SFR ($M_{\odot} \text{ yr}^{-1}$) | R_e (kpc) | Selection |
|-------------------|----------------|-----------------|------------------|-------------------|-------------------|-------------------|------------------|--|-----------------|-----------|
| GHZ1 | 3.511929 | -30.371848 | 26.36 ± 0.05 | 10.53 | 10.63 | -20.98 ± 0.06 | -1.99 ± 0.10 | 25_{-16}^{+68} | 0.43 ± 0.02 | (1), (2) |
| GHZ2 ^b | 3.498985 | -30.324771 | 27.21 ± 0.20 | 12.11 | 12.30 | -21.19 ± 0.20 | -3.00 ± 0.12 | 20_{-13}^{+14} | 0.12 ± 0.01 | (2) |
| GHZ3 | 3.528937 | -30.363811 | 26.73 ± 0.07 | 2.69 | 9.33 | -20.69 ± 0.09 | -1.85 ± 0.17 | 31_{-8}^{+10} | 0.88 ± 0.09 | (1), (2) |
| GHZ4 | 3.513743 | -30.351554 | 27.74 ± 0.12 | 10.08 | 9.93 | -19.98 ± 0.27 | -2.86 ± 0.55 | 5_{-3}^{+19} | 0.39 ± 0.09 | (1), (2) |
| GHZ5 | 3.494437 | -30.307620 | 27.25 ± 0.08 | 2.49 | 9.20 | -20.17 ± 0.18 | -1.82 ± 0.33 | 18_{-15}^{+21} | 0.21 ± 0.08 | (1) |
| GHZ6 | 3.479054 | -30.314925 | 27.43 ± 0.11 | 9.85 | 9.05 | -19.66 ± 0.21 | -1.67 ± 0.38 | 10_{-8}^{+30} | 0.45 ± 0.09 | photo z |

Notes.

^a Coordinates and fluxes are from the GLASS-JWST catalog by M22; the rest-frame M_{UV} has been obtained by converting the F200W magnitude at the average photometric redshift, except for GHZ3 and GHZ5 where the only solution at $z > 9$ was used. The UV slope β is obtained by fitting the F200W, F277W, and F356W bands; the uncertainties in the fit account for photometric errors (Castellano et al. 2012). The R_e has been estimated from the F200W image by Yang et al. (2022b). Physical parameters from ZPHOT (Santini et al. 2022). The last column indicates selections (1) and (2) in Section 3, and additional photo- z candidates not meeting color selection criteria.

^b All errors are computed considering the systematic uncertainty from different photometric techniques (Section 4).

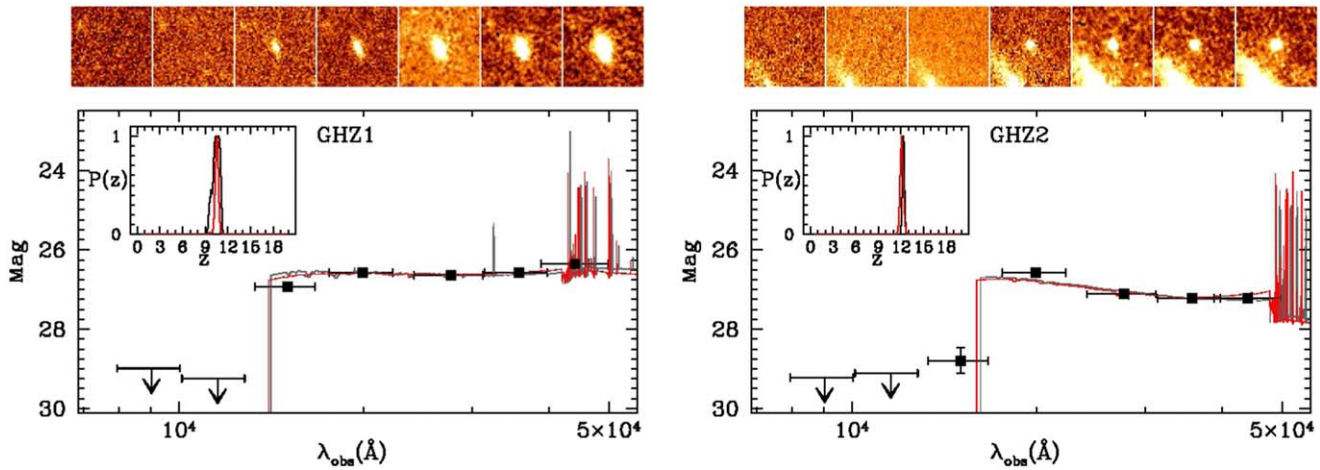


Figure 3. The two high-quality, bright high-redshift candidates from the GLASS-JWST NIRCAM field taken in parallel to NIRISS. Photometry and best-fit SEDs at the best-fit redshift are given in the main quadrant. Redshift probability distributions $P(z)$ from ZPHOT (gray) and EAZY (red) are shown in the inset. Upper limits are reported at the 2σ level, including a conservative estimate of the error budget, especially in the bluest bands (M22). Thumbnails, from left to right, show the objects in the F090W, F115W, F150W, F200W, F277W, F356W, and F444W bands.

selected with both the 2FWHM and the $0''.2$ aperture colors, with the exception of GHZ5 whose F115W – F150W color is slightly outside the selection boundary when using the 2FWHM ones. The six selected objects have been visually inspected to ensure that they are not affected by defects such as spurious sources, stellar spikes, etc. We found that GHZ2 is very compact, and it is close ($\sim 0''.5$) to a bright, foreground galaxy that contaminates the total flux measured within the Kron ellipse. We thus estimated its total flux using the T-PHOT software (Merlin et al. 2015, 2016b), which has been shown to provide accurate photometry for blended sources. We used the GHZ2 light profile in the F277W band, which provides the best compromise between resolution, S/N, and contamination from the low-redshift neighbor, as a high-resolution prior to reextract the F444W photometry. We found a total magnitude $F444W = 27.21 \pm 0.04$. Finally, we have used GALFIT (Peng et al. 2010) to fit its light profile in both the F200W and F444W bands in order to measure its spatial extent and to further assess the measurement of the total flux under different assumptions. We used a Sersic (1968) model and fixed the index n at different values from $n = 0.5$ to $n = 4$. We found that GHZ2 is compact but resolved, with effective radius 1.0 ± 0.5 pixels.

The $n = 1$ fit provides the best residuals. We found from GALFIT a total F444W magnitude of $F444W = 27.25 \pm 0.20$, in agreement with the T-PHOT measurement but with a larger error due to the systematic uncertainty on the profile parameters. We adopt this conservative error estimate in the forthcoming analysis.

Table 1 also reports the UV rest-frame magnitudes estimated from the observed F200W at the median photometric redshift, the UV slope obtained by a fit on the observed F200W, F277W, and F356W bands, the effective radius (Yang et al. 2022b), and the SFR from the SED fitting performed with ZPHOT (Santini et al. 2022). We show in Figures 3 and 4 the best-fit SEDs, the probability density function (z), and thumbnails for all candidates.

We highlight the detection of the two bright sources GHZ1 and GHZ2, at $z \simeq 10.6$ and $z \simeq 12.2$, respectively. These objects are located in the color-color diagram fairly away from color selection borders, and have no significant low-redshift solution. Their $P(z)$ is single peaked, the 68% confidence level photometric redshift range being $z_{\text{phot}} = 9.68\text{--}11.15$ ($z_{\text{EAZY}} = 10.28\text{--}10.80$) for GHZ1, and $z_{\text{phot}} = 12.03\text{--}12.58$ ($z_{\text{EAZY}} = 11.85\text{--}12.39$) for GHZ2. They are among the most

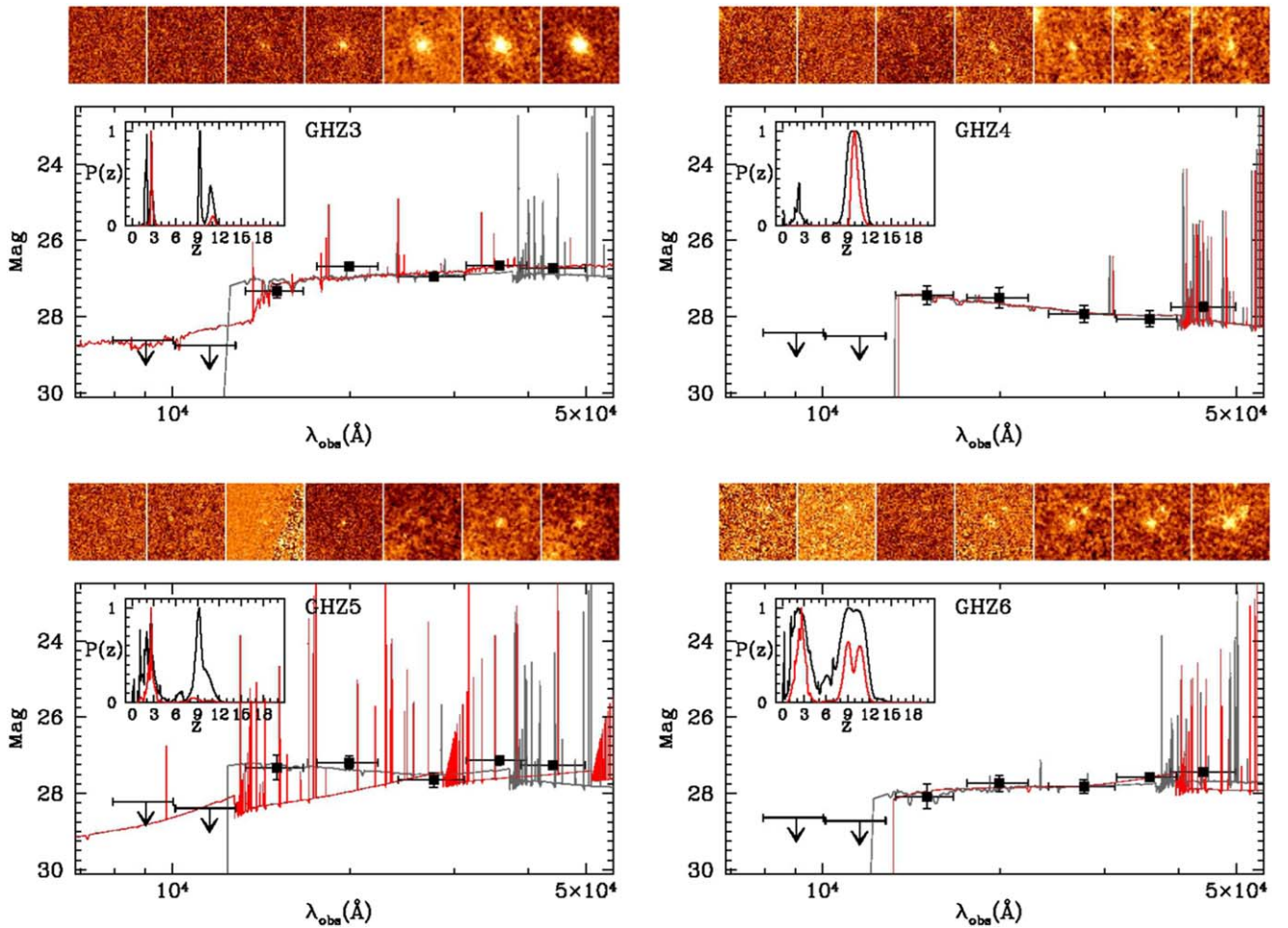


Figure 4. As in Figure 3, for fainter high-redshift candidates from GLASS-JWST. These candidates need further verification owing to the nonnegligible probability of a low-redshift solution.

robust candidates at $z > 9$ ever detected, as demonstrated by the several recent works that have presented their selection with redshift and properties comparable to those discussed here (Donnan et al. 2022; Harikane et al. 2022b; Naidu et al. 2022). They are remarkably bright ($M_{UV} \lesssim -21$) and star forming ($SFR \gtrsim 20 M_{\odot} \text{ yr}^{-1}$). GHZ2 is compact with $R_e = 120 \pm 10$ pc (Yang et al. 2022b), and it has a very steep UV slope $\beta = -3.0$. This extreme value is partly driven by the F200W band, as the slope value is $\beta = -2.4 \pm 0.2$ when using the F277W and F356W bands only. These UV slope estimates are anyway indicative of very young ages and very-low-metallicity, possibly pristine, stellar populations, which will need to be confirmed through JWST spectroscopy. A third bright candidate (GHZ3, $M_{UV} \sim -20.7$, $SFR \sim 30 M_{\odot} \text{ yr}^{-1}$) is also selected by both of our color diagrams, but its photometric redshift is more uncertain: it is found to be at $z \sim 9.3$ by ZPHOT, while EAZY gives a best-fit solution at $z \sim 2.7$. The remaining candidates are fainter ($M_{UV} \gtrsim -20.2$) galaxies likely at $z \sim 9-10$.

The GHZ3-6 candidates exhibit in general alternative lower- z solutions with nonnegligible probability. These lower- z solutions are driven in part by our conservative error estimates, especially in the bluer bands, accounting for data reduction and calibration systematics (M22). However, definitive confirmation will require deep imaging at shorter wavelengths. Instead, the contamination from galactic stars can be excluded because

all objects show resolved profiles as discussed by Yang et al. (2022b).²⁵

The physical properties, morphology, and size of our candidates are discussed in detail in the companion papers by Santini et al. (2022), Treu et al. (2022), and Yang et al. (2022b) respectively.

5. Summary and Discussion

We have presented a search for galaxy candidates at $z \sim 9-15$ from the seven-band, $\text{mag} \sim 29$ (5σ) NIRCcam imaging observations, acquired by the GLASS-JWST Early Release Science Program in parallel with NIRISS primary observations of the cluster A2744. The NIRCcam images enable the first multiband selection of Lyman-break candidates at $z \sim 9-15$ through two independent color-color diagrams.

We have identified two bright ($M_{UV} \simeq -21$) sources that, thanks to the depth of our images, are unambiguously placed at $z = 10.6$ and $z \simeq 12.2$, respectively. These are among the most reliable candidates ever selected at $z > 9$ via photometric techniques.

We have also identified five other fainter candidates at $z > 9$. Some of these objects have significant alternative solutions at

²⁵ Reassuringly, the candidate T-dwarf star GLASS-JWST-BD1 found in the GLASS-JWST-ERS field by Nonino et al. (2022) is not selected by any of our criteria.

Table 2
Predictions on the Number of $z > 9$ Objects in GLASS-JWST-ERS^a

| UV LF | $z = 9-11$ | | $z > 11$ | |
|-------------------------------|------------------------|---------------------|-----------------------|------------------------|
| | $M_{UV} < -21.0$ | $M_{UV} < -19.5$ | $M_{UV} < -21.0$ | $M_{UV} < -19.5$ |
| Oesch+18 ^b | <0.06 | $1.7^{+1.1}_{-0.6}$ | <0.04 | $0.6^{+0.5}_{-0.3}$ |
| LF(z) Bouwens+21 ^c | " | " | <0.01 | $0.1^{+0.1}_{-0.05}$ |
| Mason+15 ^d | $0.16^{+0.07}_{-0.05}$ | $6.8^{+2.9}_{-1.8}$ | 0.002 ± 0.001 | $0.08^{+0.06}_{-0.03}$ |
| Bowler+20 ^e | $0.06^{+0.30}_{-0.03}$ | $2.4^{+1.6}_{-1.9}$ | $0.05^{+0.1}_{-0.04}$ | $0.5^{+0.3}_{-0.2}$ |

Notes.

^a Uncertainties on the predicted numbers are based on the 68% c.l. errors on the Schechter parameters.

^b UV LF at $z \sim 10$ by Oesch et al. (2018), assumed fixed at $z > 11$.

^c Extrapolation at $z > 11$ of the UV LF as a function of redshift by Bouwens et al. (2021).

^d The semiempirical UV LF model by Mason et al. (2015).

^e Extrapolation of the DPL model as a function of redshift by Bowler et al. (2020).

lower redshift, that it is difficult to exclude given the limits that are currently achieved by our data, and residual systematic uncertainties especially in the bluest bands. Definitive confirmation will require deeper images at short wavelengths as well as NIRSpec spectroscopic follow-up.

Keeping in mind the uncertainties associated with our limited area and to the presence of a foreground cluster that may boost the luminosity of our candidates, it is intriguing to explore the potential implications of our results on the evolution of galaxies at large redshift.

Noting that the F444W ~ 28.2 limit corresponds to $M_{UV} \lesssim -19.5$ (-19.5) at $z = 10(13)$, we estimate the average number of sources expected in our field under several assumptions about the evolution of the LF.

At $z \sim 9-11$, we expect $1.7^{+1.1}_{-0.6}$ on the basis of the $z \sim 9$ and $z \sim 10$ UV LFs by Bouwens et al. (2021) and Oesch et al. (2018), respectively, where the uncertainties consider the relevant 68% c.l. confidence range in the LF parameters. The double power-law (DPL) model by Bowler et al. (2020) predicts $2.4^{+1.6}_{-1.9}$ galaxies. We expect as many as $6.8^{+2.9}_{-1.8}$ objects at $z \sim 9-11$ on the basis of the model by Mason et al. (2015).

At $z > 11$, where no direct constraints exists, we can estimate the average number of sources with $M_{UV} < -19.5$ under four scenarios. In the first (optimistic) case, we assume that the $z = 10$ UV LF remains constant up to $z = 15$ and predict $0.6^{+0.5}_{-0.3}$ objects in one GLASS-JWST-ERS parallel field. A perhaps more realistic scenario is provided by the evolving UV LF by Bouwens et al. (2021) that extrapolates at $z > 11$ the observed evolution in the Schechter (1976) parameters of the UV LFs measured at lower redshifts. In this second scenario, on average, only $0.1^{+0.1}_{-0.05}$ objects fall within one NIRCAM parallel field. A similar number of $0.08^{+0.06}_{-0.03}$ objects is predicted based on Mason et al. (2015). Finally, the extrapolation at $z = 11-15$ of the evolving DPL model by Bowler et al. (2020) predicts $0.5^{+0.3}_{-0.2}$ objects.

We note that such predictions are affected by cosmic variance at the level of $\sim 40\%$.²⁶ We also note that the adopted M_{UV} limits may be altered by photometric scatter. In combination with the steep increase in the number counts beyond the knee of the LF, a nonnegligible number of fainter sources can thus be scattered within the observable range. As a reference, by adopting 0.5 mag fainter M_{UV} cuts, the predicted number of objects at $z \sim 9-11$ increases to 3.5 on the basis of

the observed UV LFs, and to 7.5 in the Mason et al. (2015) model. The predicted number of sources at $z > 11$ increases to 1.5 (0.2) assuming a constant (evolving) UV LF as above, and to 0.26 on the basis of Mason et al. (2015).

Considering the incompleteness of our sample, as estimated above, we conclude that the total number of detected sources is roughly in line with the expectations of a nonevolving LF.

What is most remarkable of this first search is that we have found two bright ($M_{UV} \lesssim -21$) sources, one at $z \sim 10$ and one at $z \sim 12$, well beyond the expectations based on the extrapolation of the LF at lower redshift. In fact, all observations and models predict a negligible number of sources brighter than this limit in the redshift range $z = 9-15$ on an area equal to the GLASS one: the predictions being of $\lesssim 0.2$ objects, compared to an observed number of $2^{+2.7}_{-1.4}$ (where the uncertainty includes both cosmic variance and the Poisson uncertainty for a small number of events computed following Gehrels 1986). The aforementioned predictions are summarized in Table 2. Clearly it is premature to draw broad conclusion based on a single field, considering small number statistics, cosmic variance, clustering, and lensing. In particular, the impact of lensing on these results will need to be assessed. A preliminary investigation (based on the model by Bergamini et al. 2022) suggests that magnification may be 2–10 times higher than the 10%–15% value measured in the HFF Abell2744 Parallel (Castellano et al. 2016a). At the present stage, this indication is highly uncertain because it is extrapolated from the cluster core to the NIRCAM field 3' away, and most importantly, it is not possible to obtain lensing constraints for single sources. We note that our candidates do not show any evidence of being sheared, so although magnification of up to 50% is possible, it is unlikely to be much higher. A thorough analysis will be performed upon availability of additional spectroscopic information in the GLASS-JWST-ERS field. Despite the aforementioned sources of uncertainty, these results show that JWST can obtain the scientific results it has been designed for.

There is no doubt that the deeper and/or wider surveys already planned will eventually gather the long-awaited-for sample of galaxies in the reionization epoch and revise our understanding of how and when bright galaxies formed.

This first JWST-based search for candidate galaxies also provides us with compelling targets for spectroscopic follow-up in JWST Cycle-2. In addition to providing the necessary redshift confirmation, the relatively high luminosity of these galaxies means that NIRSpec spectroscopy should enable the





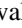






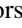













²⁶ Following the Cosmic Variance Calculator at <https://www.ph.unimelb.edu.au/~mtrenti/cvc/CosmicVariance.html>. See Trenti & Stiavelli (2008).

study of their physical properties such as SFR, dust content, and gas metallicity.

This work is based on observations made with the NASA/ESA/Canadian Space Agency James Webb Space Telescope. The data were obtained from the Mikulski Archive for Space Telescopes at the Space Telescope Science Institute, which is operated by the Association of Universities for Research in Astronomy, Inc., under NASA contract NAS 5-03127 for JWST. These observations are associated with program JWST-ERS-1324. The JWST data used in this paper can be found on MAST: [10.17909/fqag-p393](https://mast.stsci.org/#/query/10.17909/fqag-p393). We acknowledge financial support from NASA through grants JWST-ERS-1342. K.G. and T. N. acknowledge support from Australian Research Council Laureate Fellowship FL180100060. C.M. acknowledges support by the VILLUM FONDEN under grant 37459. The Cosmic Dawn Center (DAWN) is funded by the Danish National Research Foundation under grant DNRF140. We acknowledge support from INAF Minigrant “Reionization and fundamental cosmology with high-redshift galaxies.” We thank Pascal Oesch and Rohan Naidu for the useful feedback and discussion.

Software: Astropy (Astropy Collaboration et al. 2013), EAZY (Brammer et al. 2008), Empirical Galaxy Generator (Schreiber et al. 2017b), Matplotlib (Hunter 2007), SExtractor (v2.8.6 Bertin & Arnouts 1996; Guo et al. 2013), T-PHOT (Merlin et al. 2015, 2016b), zphot (Fontana et al. 2000).

ORCID iDs

Marco Castellano  <https://orcid.org/0000-0001-9875-8263>
 Adriano Fontana  <https://orcid.org/0000-0003-3820-2823>
 Tommaso Treu  <https://orcid.org/0000-0002-8460-0390>
 Paola Santini  <https://orcid.org/0000-0002-9334-8705>
 Emiliano Merlin  <https://orcid.org/0000-0001-6870-8900>
 Nicha Leethochawalit  <https://orcid.org/0000-0003-4570-3159>
 Michele Trenti  <https://orcid.org/0000-0001-9391-305X>
 Eros Vanzella  <https://orcid.org/0000-0002-5057-135X>
 Uros Mestric  <https://orcid.org/0000-0002-0441-8629>
 Mario Nonino  <https://orcid.org/0000-0001-6342-9662>
 Diego Paris  <https://orcid.org/0000-0002-7409-8114>
 Guido Roberts-Borsani  <https://orcid.org/0000-0002-4140-1367>
 Kristan Boyett  <https://orcid.org/0000-0003-4109-304X>
 Maruša Bradač  <https://orcid.org/0000-0001-5984-0395>
 Antonello Calabrò  <https://orcid.org/0000-0003-2536-1614>
 Karl Glazebrook  <https://orcid.org/0000-0002-3254-9044>
 Claudio Grillo  <https://orcid.org/0000-0002-5926-7143>
 Sara Mascia  <https://orcid.org/0000-0002-9572-7813>
 Charlotte Mason  <https://orcid.org/0000-0002-3407-1785>
 Amata Mercurio  <https://orcid.org/0000-0001-9261-7849>
 Takahiro Morishita  <https://orcid.org/0000-0002-8512-1404>
 Themiya Nanayakkara  <https://orcid.org/0000-0003-2804-0648>
 Laura Pentericci  <https://orcid.org/0000-0001-8940-6768>
 Piero Rosati  <https://orcid.org/0000-0002-6813-0632>
 Benedetta Vulcani  <https://orcid.org/0000-0003-0980-1499>
 Xin Wang  <https://orcid.org/0000-0002-9373-3865>
 Lilan Yang  <https://orcid.org/0000-0002-8434-880X>

References

- Astropy Collaboration, Robitaille, T. P., Tollerud, E. J., et al. 2013, *A&A*, **558**, A33
- Atek, H., Richard, J., Kneib, J.-P., & Schaerer, D. 2018, *MNRAS*, **479**, 5184
- Bagley, M. B., Finkelstein, S. L., Rojas-Ruiz, S., et al. 2022, arXiv:2205.12980
- Bergamini, P., Acebron, A., Grillo, C., et al. 2022, arXiv:2207.09416
- Bertin, E., & Arnouts, S. 1996, *A&AS*, **117**, 393
- Bouwens, R. J., Illingworth, G. D., van Dokkum, P. G., et al. 2022, *ApJ*, **927**, 81
- Bouwens, R. J., Oesch, P. A., Stefanon, M., et al. 2021, *AJ*, **162**, 47
- Bowler, R. A. A., Jarvis, M. J., Dunlop, J. S., et al. 2020, *MNRAS*, **493**, 2059
- Brammer, G. B., van Dokkum, P. G., & Coppi, P. 2008, *ApJ*, **686**, 1503
- Bruzual, G., & Charlot, S. 2003, *MNRAS*, **344**, 1000
- Calzetti, D., Armus, L., Bohlin, R. C., et al. 2000, *ApJ*, **533**, 682
- Castellano, M., Amorín, R., Merlin, E., et al. 2016a, *A&A*, **590**, A31
- Castellano, M., Fontana, A., Grazian, A., et al. 2012, *A&A*, **540**, A39
- Castellano, M., Sommariva, V., Fontana, A., et al. 2014, *A&A*, **566**, A19
- Castellano, M., Yue, B., Ferrara, A., et al. 2016b, *ApJL*, **823**, L40
- Coe, D., Zitrin, A., Carrasco, M., et al. 2013, *ApJ*, **762**, 32
- Dayal, P., & Ferrara, A. 2018, *PhR*, **780**, 1
- Dayal, P., Volonteri, M., Choudhury, T. R., et al. 2020, *MNRAS*, **495**, 3065
- Donnan, C. T., McLeod, D. J., Dunlop, J. S., et al. 2022, arXiv:2207.12356
- Finkelstein, S. L., Bagley, M., Song, M., et al. 2022, *ApJ*, **928**, 52
- Finkelstein, S. L., D’Aloisio, A., Paardekooper, J.-P., et al. 2019, *ApJ*, **879**, 36
- Finkelstein, S. L., Ryan, R. E., Jr., Papovich, C., et al. 2015, *ApJ*, **810**, 71
- Fontana, A., D’Odorico, S., Poli, F., et al. 2000, *AJ*, **120**, 2206
- Fontana, A., Dunlop, J. S., Paris, D., et al. 2014, *A&A*, **570**, A11
- Gehrels, N. 1986, *ApJ*, **303**, 336
- Giavalisco, M. 2002, *ARA&A*, **40**, 579
- Grazian, A., Castellano, M., Fontana, A., et al. 2012, *A&A*, **547**, A51
- Greig, B., & Mesinger, A. 2017, *MNRAS*, **465**, 4838
- Guo, Y., Ferguson, H. C., Giavalisco, M., et al. 2013, *ApJS*, **207**, 24
- Hainline, K. N., Hviding, R. E., Rieke, M., et al. 2020, *ApJ*, **892**, 125
- Harikane, Y., Inoue, A. K., Mawatari, K., et al. 2022a, *ApJ*, **929**, 1
- Harikane, Y., Ouchi, M., Oguri, M., et al. 2022b, arXiv:2208.01612
- Hashimoto, T., Laporte, N., Mawatari, K., et al. 2018, *Natur*, **557**, 392
- Hunter, J. D. 2007, *CSE*, **9**, 90
- Ishigaki, M., Kawamata, R., Ouchi, M., et al. 2018, *ApJ*, **854**, 73
- Jiang, L., Kashikawa, N., Wang, S., et al. 2021, *NatAs*, **5**, 256
- Kawamata, R., Ishigaki, M., Shimasaku, K., et al. 2018, *ApJ*, **855**, 4
- Kron, R. G. 1980, *ApJS*, **43**, 305
- Leethochawalit, N., Trenti, M., Santini, P., et al. 2022, arXiv:2207.11135
- Lotz, J., Mountain, M., Grogan, N. A., et al. 2014, *AAS Meeting*, **223**, 254.01
- Marley, M. S., Saumon, D., Visscher, C., et al. 2021, *ApJ*, **920**, 85
- Mason, C. A., Trenti, M., & Treu, T. 2015, *ApJ*, **813**, 21
- Mason, C. A., Treu, T., de Barros, S., et al. 2018, *ApJL*, **857**, L11
- McLeod, D. J., McLure, R. J., Dunlop, J. S., et al. 2015, *MNRAS*, **450**, 3032
- McLeod, D. J., McLure, R. J., & Dunlop, J. S. 2016, *MNRAS*, **459**, 3812
- McLure, R. J., Dunlop, J. S., Bowler, R. A. A., et al. 2013, *MNRAS*, **432**, 2696
- Merlin, E., Bonchi, A., Paris, D., et al. 2022, arXiv:2207.11701
- Merlin, E., Amorín, R., Castellano, M., et al. 2016a, *A&A*, **590**, A30
- Merlin, E., Bourne, N., Castellano, M., et al. 2016b, *A&A*, **595**, A97
- Merlin, E., Castellano, M., Santini, P., et al. 2021, *A&A*, **649**, A22
- Merlin, E., Fontana, A., Ferguson, H. C., et al. 2015, *A&A*, **582**, A15
- Merlin, E., Fortuni, F., Torelli, M., et al. 2019, *MNRAS*, **490**, 3309
- Mitra, S., Choudhury, T. R., & Ferrara, A. 2015, *MNRAS*, **454**, L76
- Morishita, T., Trenti, M., Stiavelli, M., et al. 2018, *ApJ*, **867**, 150
- Naidu, R. P., Oesch, P. A., van Dokkum, P., et al. 2022, arXiv:2207.09434
- Nonino, M., Glazebrook, K., Burgasser, A. J., et al. 2022, arXiv:2207.14802
- Oesch, P. A., Bouwens, R. J., Illingworth, G. D., Labbé, I., & Stefanon, M. 2018, *ApJ*, **855**, 105
- Oesch, P. A., Brammer, G., van Dokkum, P. G., et al. 2016, *ApJ*, **819**, 129
- Oesch, P. A., Labbé, I., Bouwens, R. J., et al. 2013, *ApJ*, **772**, 136
- Oke, J. B., & Gunn, J. E. 1983, *ApJ*, **266**, 713
- Ono, Y., Ouchi, M., Harikane, Y., et al. 2018, *PASJ*, **70**, S10
- Peng, C. Y., Ho, L. C., Impey, C. D., & Rix, H.-W. 2010, *AJ*, **139**, 2097
- Reddy, N. A., & Steidel, C. C. 2009, *ApJ*, **692**, 778
- Roberts-Borsani, G., Morishita, T., Treu, T., Leethochawalit, N., & Trenti, M. 2022a, *ApJ*, **927**, 236
- Roberts-Borsani, G., Morishita, T., Treu, T., et al. 2022b, arXiv:2207.11387
- Roberts-Borsani, G. W., Bouwens, R. J., Oesch, P. A., et al. 2016, *ApJ*, **823**, 143
- Rojas-Ruiz, S., Finkelstein, S. L., Bagley, M. B., et al. 2020, *ApJ*, **891**, 146
- Salpeter, E. E. 1955, *ApJ*, **121**, 161
- Santini, P., Fontana, A., Castellano, M., et al. 2022, arXiv:2207.11379

- Schaerer, D., & de Barros, S. 2009, *A&A*, 502, 423
- Schechter, P. 1976, *ApJ*, 203, 297
- Schmidt, M. 1963, *Natur*, 197, 1040
- Schreiber, C., Elbaz, D., Pannella, M., et al. 2017a, *A&A*, 602, A96
- Schreiber, C., Pannella, M., Leiton, R., et al. 2017b, *A&A*, 599, A134
- Sersic, J. L. 1968, *Atlas de Galaxias Australes* (Cordoba: Observatorio Astronomico)
- Trenti, M., & Stiavelli, M. 2008, *ApJ*, 676, 767
- Treu, T., Calabro, A., Castellano, M., et al. 2022, arXiv:2207.13527
- Treu, T., Roberts-Borsani, G., Bradac, M., et al. 2022, *ApJ*, 935, 110
- Vulcani, B., Trenti, M., Calvi, V., et al. 2017, *ApJ*, 836, 239
- Williams, C. C., Curtis-Lake, E., Hainline, K. N., et al. 2018, *ApJS*, 236, 33
- Yang, L., Leethochawalit, N., Treu, T., et al. 2022a, *MNRAS*, 514, 1148
- Yang, L., Morishita, T., Leethochawalit, N., et al. 2022b, arXiv:2207.13101
- Yue, B., Castellano, M., Ferrara, A., et al. 2018, *ApJ*, 868, 115
- Zheng, W., Postman, M., Zitrin, A., et al. 2012, *Natur*, 489, 406